Wintertime Evolution of Landfast Ice Stability in Alaska from InSAR

Andrew Einhorn[1,2,3] and Andrew Mahoney[1]

[1]Geophysical Institute, University of Alaska Fairbanks, Fairbanks, 99775, United States of America
[2]Institute for Marine and Antarctic Studies, University of Tasmania, Hobart, 7001, Australia
[3]Australia Antarctic Program Partnership, Institute for Marine and Antarctic Studies, University of Tasmania, Hobart, 7001, Australia

Correspondence: Andrew Einhorn (andrew.einhorn@utas.edu.au)

Abstract. Landfast ice in Alaska is experiencing rapid changes in extents and duration, impacting the safety and utility of the ice for Arctic coastal communities. Current datasets of landfast ice only distinguish landfast ice from mobile pack ice, omitting crucial information regarding the relative safety within landfast ice. InSAR (Interferometric Synthetic Aperture Radar) holds promise for identification of landfast ice and measurement of cm-scale deformation from a spaceborne sensor. We use two properties of interferometry: coherence to identify areas of landfast ice, and the interferometric phase gradient to approximate a new metric called apparent strain (ϵ_a) which acts as a proxy for estimating the relative stability of the landfast ice. Apparent strain is described as the horizontal gradient of interferometric phase in the line-of-sight displacement. We built on a previous study by Dammann et al. (2019) by assigning quantitative apparent strain values to identify 3 distinct stability classifications of landfast ice: Bottomfast ($\epsilon_a \leq 8.6 \times 10^{-6}$), Stabilized ($8.6 \times 10^{-6} < \epsilon_a \leq 2.4 \times 10^{-5}$), and Nonstabilized ($\epsilon_a > 2.4 \times 10^{-5}$). The monthly average apparent strain decreases as the season progresses, achieving the maximum stability in April or May depending on the region. This study introduces a novel approach to identify the relative stability for areas of landfast ice using InSAR. These findings have implications for enhancing the safety and planning of activities on landfast ice for Arctic coastal communities.

1 Introduction

1.1 Remote Sensing of Landfast Ice

Landfast ice, also commonly referred to as fast ice or shorefast ice, is sea ice that has become fastened to the coast and remains stationary for a period of time (Barry et al., 1979). Landfast sea ice is the most commonly encountered form of sea ice due to its proximity to Arctic coastal communities and its relative safety compared to drifting sea ice. Members of Arctic coastal communities use landfast ice for subsistence hunting and intercommunity travel, among other uses (e.g., George et al. (2004); Laidre et al. (2008)). Landfast ice also serves as a habitat for marine mammals and shore birds (Laidre et al. (2015); Lovvorn et al. (2014)) and can be used for industrial purposes (Bieniek et al. (2022); Masterson (2009)). As a rigid barrier between the ocean and land, landfast ice can mitigate coastal erosion (Hošeková et al., 2021) and modify large-scale

circulation patterns (Itkin et al., 2015; George et al., 2004; Laidre et al., 2008). The fundamental property of landfast ice that allows it to perform all these roles in the Earth system is its attachment to the land. Mahoney et al. (2006) proposed that this attachment could be determined from remote sensing data using two criteria: contiguity with the coast and immobility over time. Coastal contiguity can be determined from any single image with sufficient resolution to observe meaningful leads of open water, but determination of immobility requires at least two images of the same area acquired at different times. For example, Mahoney et al. (2007, 2014) analyzed triplets of co-located synthetic aperture radar (SAR) data spanning approximately 20 days to identify landfast ice in Alaska, while Fraser et al. (2012, 2020, 2021) and Cooley and Ryan (2024) derived landfast ice extent from 20- and 30-day composites of cloud-free moderate resolution imaging spectrometer (MODIS) data. Landfast ice is also identified in operational ice charts based on analysis of multiple images utilizing a range of satellite based sensing methods (World Meteorological Organization, 2014). These various techniques of remote sensing produce similar analysis of the landfast ice in that the data is presented as a binary presence or absence of landfast ice within a grid cell. While these techniques useful and valid for mapping landfast ice, the utility of landfast ice does not solely rely on the presence of fast ice but also the safety and stability. Interferometric Synthetic Aperture Radar (InSAR) has been shown to not only delineate landfast ice from mobile pack ice, but also measure centimeter to millimeter scale deformation within the fast ice (Dammann et al., 2016, 2018a, 2019; Dammert et al., 1998; Fedders et al., 2024; Li et al., 1996; Meyer et al., 2011; Morris et al., 1999).

1.2 Interferometric Coherence

Interferometric coherence ($\hat{\gamma}$), derived from spaceborne sensors, is a necessary condition for processing SAR pairs using interferometry and is generally only maintained over landfast ice not mobile pack ice between repeat orbits. Interferometric coherence is the measure of correlation between the two phase signals of the same area acquired at different times (temporal baseline) and orbit positions (perpendicular baseline). Thresholding interferometric coherence to delineate landfast ice from mobile pack ice has been done before with the the L-band ($\lambda = 23.6cm$) sensor Phased Array type L-band Synthetic Aperture Radar (PALSAR) aboard the Japanese satellite Advanced Land Observing Satellite (ALOS) (Meyer et al., 2011). The low frequency of PALSAR allowed for landfast ice to maintain coherence over long periods (~ 46 days). The L-band wavelength of PALSAR allows the signal to be more resilient to decorrelating. Decorrelation, reductions of coherence, is likely the result of a combination of:

- errors in coregistration of the SAR images ($\gamma_{\text{processes}}$)
- changes in incidence angle (γ_{spatial})
- changes in the dielectric properties of the surface (γ_{thermal})
- and deformation of the surface (γ_{temporal})

Examples of processes specific to sea ice which reduce coherence are redistribution of snow, melting and refreezing of the surface, ice deformation and motion, and rapid changes in salinity. Meyer et al. (2011) found that areas independently identified as mobile pack ice had an mean coherence ≤ 0.08, indicating total decorrelation while areas of landfast ice has a mean

coherence of ~ 0.29 with an L-band SAR sensor. This analysis lead Meyer et al. (2011) to define -pixels which maintained normalized coherence values ≥ 0.1 over a 46 day period were classes as landfast. In addition, morphological filtering was needed to remove spurious non-contiguous pixels returning a coherence value ≥ 0.1. Meyer et al. (2011) did note that even with L-band, coherence was poor over thin landfast ice and the after the onset of spring melt. Similarly when using the shorter wavelength C-band ($\lambda = 5.6cm$) SAR senor aboard Sentinel-1, Dammann et al. (2019) observed generally poor coherence in the along the Alaska coastline in the Chukchi Sea due to suspected thin landfast ice and surface melting. Using Sentinel-1 Dammann et al. (2019) used the boundary between zero and nonzero coherence to identify the landfast ice edge. Both Meyer et al. (2011) and Dammann et al. (2019) selected SAR pairs from winter months (December - May) to maximize landfast ice extent and thickness while reducing the impacts of melt onset thus maximizing coherence. Coherence is required to perform interferometry between two SAR signals. Without coherence, phase, and thus deformation, can not be measured accurately.

1.2.1 Interferometric Phase

The interferometric phase is one of the core measurements derived from interferometry as it can represented the amount of deformation which has occurred between signal acquisitions. The phase difference between SAR images is often called the interferometric phase, ϕ, primarily results from the effects of surface topography when viewed from two different positions, or line-of-sight surface displacement which occurred between image acquisitions when viewed from similar positions. Over sea ice, where topographic expression is generally low, $< 10m$, variations in ϕ can be expected to be dominated by surface motion (Bamler and Hartl, 1998; Ferretti et al., 2007). Deformation in the across-track and vertical directions result in a phase change while InSAR is not sensitive to deformation which occurs parallel to the orbit direction, also known as along-track deformation. The interferometric phase is commonly depicted by interferograms. Traditional interferograms consist of multicolored fringes where one fringe represents half a wavelength of deformation in the line-of-sight direction. The spatial rate at which the phase changes, phase gradient ($\nabla\phi$), provides insight and a measurement of the type and magnitudes of deformation occurring within the landfast ice. $\nabla\phi$ is calculated as:

$$\nabla\phi = (\frac{\partial\phi}{\partial x}, \frac{\partial\phi}{\partial y}) \tag{1}$$

indicating the change in phase in the across-track ($\frac{\partial\phi}{\partial x}$) and vertical directions ($\frac{\partial\phi}{\partial y}$). The interferometric phase (Dammert et al., 1998), fringe patterns (Dammann et al., 2018b, 2019; Fedders et al., 2024; Morris et al., 1999; Pratt, 2022; Wang et al., 2020), phase difference (Li et al., 1996), and phase gradient (Dammann et al., 2019; Fedders et al., 2024) have been used to approximate the deformation and stability of landfast ice. Inverse modeling of landfast sea ice deformation is possible from InSAR, but requires either in-situ observations of deformation and stressors or constraining the fringe patterns to specific patterns (Dammann et al., 2016, 2018a; Fedders et al., 2024). Dammann et al. (2019) classified the deformation of landfast ice based on interferometric phase on a larger scale. They opted to directly interpret the phase information as representing the magnitude of strain rather than the inverse modeling approach which would also identify the type of strain. On large scales it is not feasible to use inverse modeling to determine the type and magnitude of strain as key data to accurately constrain the each

area are not available. For studies in which the deformation cannot be restricted, directly interpreting the interferometric phase as a measure of the deformation is preferred.

The classification of landfast ice stability by Dammann et al. (2019) demonstrated the utility of interpreting fringes to represent the stability of landfast ice, but the definitions used were qualitative thus difficult to reproduce and automate. Dammann et al. (2019) identified three stability zones based on the interferometric fringe pattern, orientation, and spacing:

- Bottomfast ice - No identifiable phase difference from the adjacent land - same definition used by Pratt (2022))
- Stabilized - Poorly defined, widely spaced fringes, or abruptly reduced fringe spacing compared to offshore ice
- Nonstabilized - Well-defined fringe orientation or patterns

While useful, these definitions can be subjective and are not easy to programmability replicate. Hence we saw a need to quantitatively defined these stability classes such that the process has the ability to be automated. We build directly on the previous work of Dammann et al. (2018b, 2019); Meyer et al. (2011); Pratt (2022) to map the extent of landfast ice and develop a method for quantitatively definition of these stability zones using interferometric data from 12 day Sentinel-1 SAR pairings. To do so we defined a new metric called apparent strain (ϵ_a) which is derived from the interferometric phase gradient. Apparent strain describes the amount of line-of-sight deformation InSAR is sensitive too which occurred between satellite acquisitions. Having quantitative definitions of the stability zones defined by Dammann et al. (2019), using apparent strain, provides the opportunity to map the extent of these stability zones and to understand their evolution both intra- and inter-seasonally.

2 Data and Methods

2.1 Study Area

Our study area was chosen to coincide with that used for the development of the EM2025 landfast ice climatology (see Section 2.2) and includes waters of the U.S. Arctic Outer Continental Shelf and adjacent waters in Canada and Russia. The coastlines extend from just west of Neshkan on the Chukotka Peninsula to the easternmost point of the Russian mainland in the Bering Strait and from the westernmost point on mainland Alaska, the Iñupiat village of Wales, to the Mackenzie Delta in Canada. To conform with prior analyses of landfast ice (Mahoney et al., 2007, 2014, 2024), our study area is divided into two regions (Fig. 1). The western region lies entirely within the Chukchi Sea and hereinafter is referred to as the Chukchi region, shaded cyan in Figure 1. The eastern region includes a smaller area of the northern Alaska Chukchi coast but is otherwise contained within the Beaufort Sea and hereinafter is referred to as the Beaufort region, blue shaded region in Figure 1. The western and eastern regions about each other at a point just west of Wainwright Alaska.

2.2 EM2025 landfast ice climatology

The EM2025 landfast ice climatology (named after the same authors as this study and the year it was released) is a gridded daily dataset of landfast ice extent covering the study area depicted in Figure 1 and extends from 1996-2023. A detailed

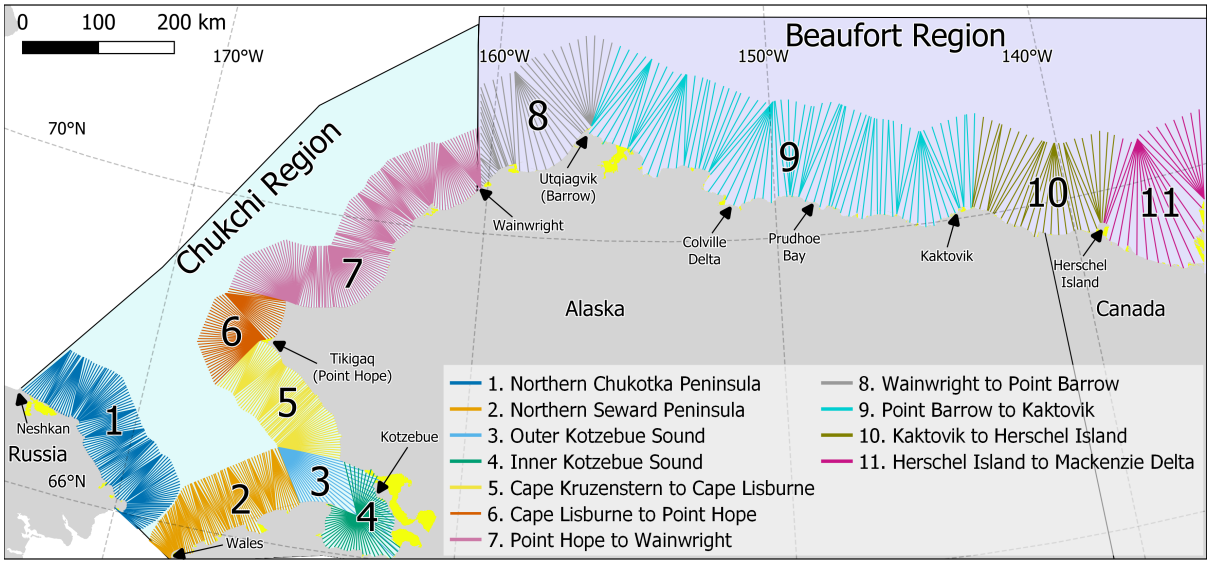

Figure 1. Spatial extent of the study area, two regions (Beaufort and Chukchi) and 11 sub regions. Every 10^{th} coast normal vector is displayed for each subregion in varying colors. Each vector is used to measure fast ice extent for both the InSAR method and EM2025 data. Yellow shaded regions represent "shadow regions" discussed in Section 2.2.

description of the creation and results of the EM2025 dataset are reported by Mahoney et al. (2024) and Mahoney and Einhorn (2025) but in brief, it extends a previous SAR-based dataset of the same study area for the years 1996-2008 (Mahoney et al., 2014) using data derived from ice charts produced by National Ice Center (NIC) and the National Weather Service's Alaska Sea Ice Program (ASIP). Here, we use landfast ice width data derived from the EM2025 dataset using the SLIEalyzer toolbox (https://github.com/armahoney/SLIEalyzer), which computes the distance from the coast to the seaward landfast ice edge (SLIE) along a specified set of approximately coast-normal vectors, as illustrated in Figure 1. Regions of the coastline which are not captured by the coast vectors are termed "shadow regions" and denoted with shaded yellow regions in Figure 1 and all subsequent maps. Shadow regions occur due to complexities of the coastline such as small bays or straits where the coast normal vector would intersect another part of the main landmass. This approach provides a consistent spatial reference frame with which to measure the seasonal and inter-annual variations in landfast ice almost continuously at 8892 different locations along the coast (6956 in the Chukchi region and 1936 in the Beaufort), spaced approximately every 200 m. It also allows us to calculate various statistics about the locations of the SLIE over different time periods.

2.3 InSAR-based detection of landfast ice

The term InSAR, in this study, describes a signal processing technique for calculating the phase difference between two radar signals acquired from similar locations in space at separate times. Here, we use pairs of Sentinel-1 interferometric wide (IW) beam images with temporal and perpendicular baselines of 12 days and ≤ 300 m respectively. These image pairs were selected

using the Short Baseline Subset tool within the Alaska Satellite Facility (ASF)'s Vertex portal. 13 IW reference scenes chosen exclusively on the basis of coverage of the study region. Six reference scenes were used to cover the Beaufort region while seven were used to cover the Chukchi region. In total, 2,084 SAR pairs were identified between the months of November and July for the period from March 2017 to July 2022. These SAR scenes were multi-looked by 20x4 resulted in pixel size of 80×80 m, improving the signal to noise ratio. We used ASF's Hybrid Pluggable Processing Pipeline (HyP3) toolbox (Hogenson et al., 2016) to produce interferometric data products in GeoTIFF format.

To obtain a useful value of ϕ, the two SAR signal must have remained sufficiently coherent between Sentinel-1's repeat orbits. The HyP3 toolbox (Hogenson et al., 2016) produces normalized coherence images where values of 0 indicate complete decorrelation and 1 indicates perfect coherence (Moreira et al., 2013). The magnitude of the reduction of coherence ($|\hat{\gamma}|$) can be estimated as:

$$|\hat{\gamma}| = \gamma_{\text{processes}} \cdot \gamma_{\text{spatial}} \cdot \gamma_{\text{thermal}} \cdot \gamma_{\text{temporal}} \tag{2}$$

By limiting our spatial baseline to ≤ 300 m and assume and use constants specific to Sentinel-1 and C-band we can treat γ_{spatial} γ_{thermal} as constants. In addition we assumed that $\gamma_{\text{processes}}$ is 1, indicating there are no errors in the coregistration of the SAR pairs. These assumptions allowed us to assumed all variability in the reduction of coherence was associated with deformation/displacement of the surface γ_{temporal}.

In the context of sea ice, reductions of γ_{temporal} are assume to be caused by ice drift or deformation, which is typically on the order of km per day for mobile pack ice. For drifting pack ice over a 12-day repeat orbit interval, (γ_{temporal}) is reduced to zero, resulting in decorrelation ($|\hat{\gamma}| = 0$). Fast ice by definition is stationary, but internal deformation still causes reductions of γ_{temporal}. However, for the landfast ice to remain landfast, the magnitude of this deformation needs to be relatively small as to not cause fracturing. While the coherence will be reduced in highly dynamic landfast ice, the coherence will be higher when compared to adjacent pack ice. This principle has previously been used by Meyer et al. (2011) to delineate fast ice from fast land ice from pack ice.

Meyer et al. (2011) demonstrated the ability to delineate landfast ice from mobile pack ice using a coherence threshold and morphological filtering in Alaska. The normalized coherence threshold used by Meyer et al. (2011) when using L-band PALSAR was 0.1. For this study, we use C-band which is more sensitive to smaller changes in the surface resulting in lower coherence values. The coherence threshold used by Meyer et al. (2011) can not be simply assumed to be the same for the different wavelengths due to the increased sensitivity of C-Band. For that reason we derived a C-Band specific coherence threshold to delineate landfast ice from mobile pack ice. A more detailed description of this derivation can be found in the Supplementary Section 1. In short, we used 14 SAR pairs, one from each month between December 2017 and June 2018, form the Chukchi region and Beaufort region. The Chukchi scene covered most of the northern Seward Peninsula and some of Kotzebue Sound while the Beaufort region scene covered the coastline west of Utqiagvik until approximately the Colville Delta. We applied thresholds ranging from 0.01 through 1.00 to the coherence images then applied morphological closing and opening operations to remove small and noncontiguous areas which exceed the threshold which are likely noise. We then compared the areas identified by each threshold in each month to the extent of the minimum landfast ice extent identified in

that month by the EM2025 dataset. The best threshold was then determined by the highest percentage of pixels that agreed with the corresponding EM2025 monthly minimum extent. The coherence threshold for delineating landfast ice from the mobile pack ice using C-Band was determined to be 0.3 where areas which meet or exceeded this threshold were classified as landfast ice. This threshold was then applied to all normalized coherence images and used to measure landfast ice extent and to mask the interferograms such that we are only calculating apparent strain in the areas identified as landfast ice.

2.4 Calculation of apparent strain from phase gradient

After masking the interferograms based on the ≥ 0.3 coherence threshold we used the magnitude of the interferometric phase gradient to measure the apparent strain in each interferogram. For short-baseline 12-day SAR pairs over sea ice, we can assume that variations in interferometric phase ϕ are dominated by variations in line-of-sight surface motion, not topography. ϕ is insensitive to motion perpendicular to the line of sight, but Fedders et al. (2024), has shown that it is possible to estimate 2-dimensional horizontal strain of sea ice from the phase gradient provided the phase slope is largely planar and the mode of deformation (e.g., radial divergence or rotation) is known. However, in general, derivation of 2-D or 3-D surface motion requires phase information from multiple look directions and the known deformation type. Instead, we define the term apparent strain, (ϵ_a), to describe the magnitude of the horizontal gradient in line-of-sight displacement. Apparent strain can be calcuated using the following:

$$\epsilon_{\mathbf{a}} = \frac{\lambda}{4\pi(\mathbf{pixel\ width})} |\nabla\phi| \tag{3}$$

Where λ is the C-band SAR wavelength (5.64 cm) of Sentinel-1 and $|\nabla\phi|$ is the magnitude of the phase gradient, given by:

$$|\nabla\phi| = \frac{\sqrt{\frac{\partial\phi}{\partial x}^2 + \frac{\partial\phi}{\partial y}^2}}{(kenral\ length - 1)} \tag{4}$$

Since ϕ is a cyclic quantity that wraps over an interval of 2π, we calculate $\nabla\phi$ following the approach described by Libert et al. (2022) whereby ϕ is first converted to a complex quantity, ϕ^*, with continuous real and imaginary components:

$$\phi^* = e^{i\phi} = cos\phi + i\ sin\phi \tag{5}$$

$$\frac{\partial\phi}{\partial x} = \angle\left(\frac{\partial\phi^*}{\partial x}\right) \tag{6}$$

$$\frac{\partial\phi}{\partial z} = \angle\left(\frac{\partial\phi^*}{\partial z}\right) \tag{7}$$

Where $\angle$ indicates the argument of the complex exponent.

We approximate the partial derivatives in (Eq. 6) and (7) using finite differences across a 4-pixel window and insert into (Eq. 4) to derive the magnitude of the phase gradient magnitude. Apparent strain, ϵ_a, is then calculated using (Eq. 3) and should be

interpreted as the minimum net strain that occurred between SAR image acquisitions, since it only measures deformation along the satellite's line of site. However, since it only represents displacement between two snapshots in time, it may underestimate the maximum strain that occurred during the 12-day period. As with the coherence images, we grouped ϵ_a results by month according to the date of the primary image in each SAR pair and mosaicked results to create images of monthly average ϵ_a for each of the Chukchi and Beaufort regions.

2.5 Spatial masks for defining apparent strain thresholds for stability

The Sentinel-1 SAR pairs using by Dammann et al. (2019) along the Alaskan Beaufort coastline do not follow the same strict temporal baseline requirement of 12-days between pairs prohibiting the direct use of these SAR pair during the derivation of apparent strain thresholds for each stability class, but will be used to compare with later. To account for this, we interpreted the landfast ice regimes associated with each stability zone and created masks that reflect the characteristics of landfast ice in each zone, but are usable in all years (Fig. 2). The spatial extents for each of these masks was determined independently of apparent strain values but instead by bathymetry, geomorphology characteristics, and features of the nearshore environment. These masks, which are shown in Figure 2, represent the areas we know to fit the characteristic of each fast ice regime associated with each stability zone defined by Dammann et al. (2019). These stability zones were defined using the following criteria associated with bathymetry, geomorphology characteristics, and features:

1. Bottomfast Landfast Ice (BFLFI) - Areas of the near shore environment with a water depth shallower than 1.5 m (Danielson et al., 2015)

2. Sheltered Landfast Ice (SHLFI) - Areas between the seaward edge of the BFLFI edge and shoreward of any barrier island. We acknowledge that barrier islands are not the only feature which anchor landfast ice.

3. Not Sheltered Landfast Ice (NSHLFI) - Areas where landfast ice occurs seaward of barrier island.

The bounds of the BFLFI mask were determined to be the area where water depth is between 0 m and 1.5 meters as these are the typical depth bottomfast ice is found (Pratt, 2022). It is also important to acknowledge the difference between sheltered and stabilized terminologies in this instance. Sheltered landfast ice (SHLFI) is specifically landfast ice which is floating and anchored by barrier islands. The barrier islands shelter this landfast ice from dynamic interactions with waves and pack ice. SHLFI is likely to exhibit greater stability (lower apparent strain) compared to landfast ice anchored by grounded ridges, as barrier islands can better isolate landfast ice from ocean dynamics. The definition of the stabilized landfast ice zone by Dammann et al. (2019) includes landfast ice anchored by both barrier islands and grounded ridges. However, due to the location of grounded ridges not being consistent between seasons, we opted to use the areas sheltered only by barrier island, SHLFI, as a representative area for the determination of an apparent strain threshold of the stabilized zone defined by Dammann et al. (2019). Given this definition and spatial extent of SHLFI, we can assume that any landfast ice occurring within the SHLFI mask is anchored, thus representative of stabilized landfast ice, regardless of season. This also results in landfast ice that is grounded by ridges seaward of the barrier island to be located within the NSHLFI mask, skewing the distribution of the NSHLFI toward

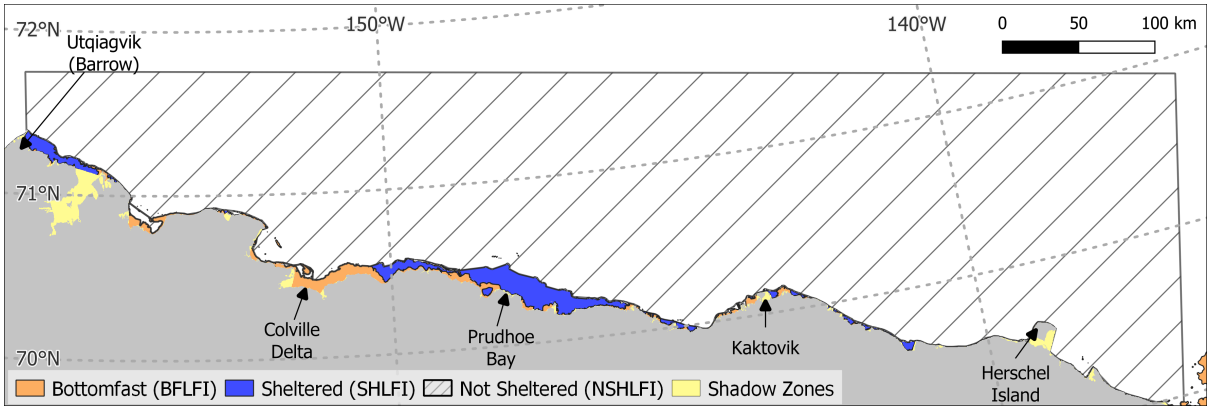

Figure 2. Spatial extent of the masks use for the derivation of the apparent strain thresholds associated with the stability zones from Dammann et al. (2019). Orange areas are bottomfast, blue is sheltered, and hashed black is not sheltered. Yellow shaded regions represent "shadow regions" discussed in Section 2.2.

a lower apparent strain. We then took the average of all apparent stain maps, on a per pixel basis, occurring in the Beaufort region during the month of April and derived the apparent strain thresholds for the three stability zones defined by Dammann et al. (2019) using a non-parametric optimization of the data within each mask independently.

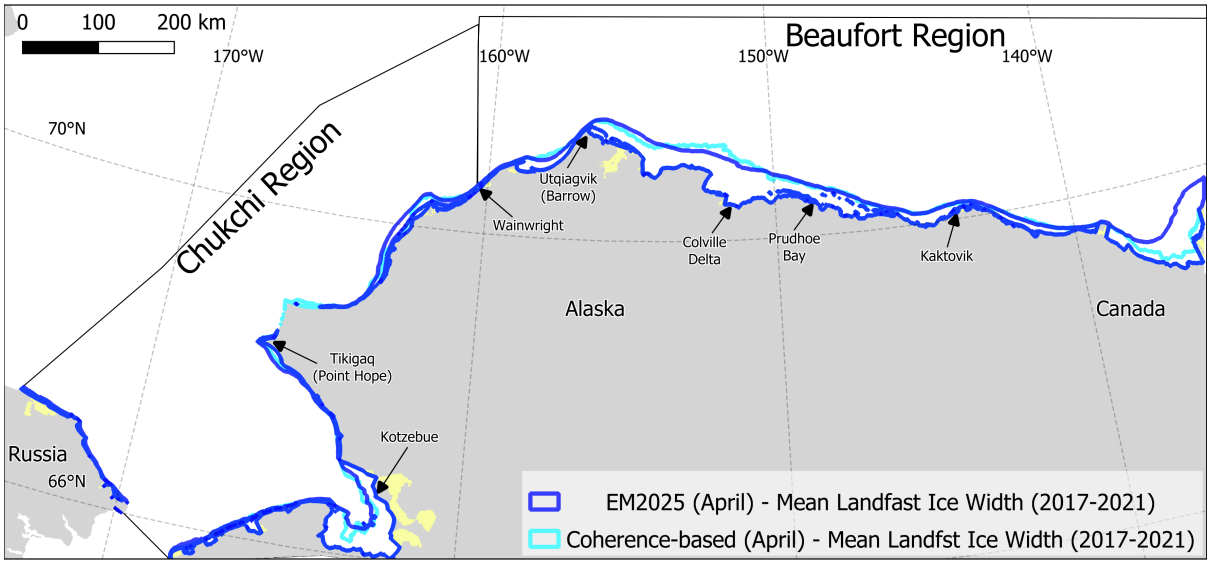

Figure 3. Spatial comparison of the April monthly mean (2017-2021) landfast ice width across the study region using the coherence based mosaics (cyan) and the EM2025 dataset (blue). Yellow regions are "shadow zones" where the coast vectors do not reach.

3 Results

3.1 Landfast ice extent from coherence thresholds

Application of the coherence threshold described in Section 2.3 to 2,084 SAR image pairs allowed us to produce 30 monthly mosaics of landfast ice for each month between December and May during the 5 landfast ice seasons between 2017 and 2021. We then used the SLIEalyzer toolbox (Section 2.2) to derive the average position of the SLIE over all 5 seasons for each month for comparison with the equivalent results derived from the EM2025 dataset. For example, Figure. 3 compares positions of the InSAR-derived mean landfast ice extent during April (blue) line with that derived from the EM2025 dataset (cyan) for the period 2017-2021. This shows a generally good agreement, with no consistent bias in the study region for this month. However, when averaging the difference between methods, the coherence mosaics did tend to underestimate the landfast ice extent by between 1.5 km and 5 km on average each month.

To compare the coherence-derived landfast ice extent against the EM2025 dataset for all months from December to May, we calculated the difference in monthly mean landfast ice width for each coast vector measured by the coherence-based method and the EM2025 dataset (Fig. 4). Here, the difference is calculated by subtracting the EM2025 values from the coherence-derived width values, meaning a negative value represents an underestimate by the coherence method. Figure 4 represent then entire coastline where coast vectors from the Chukchi region are plotted in cyan while the Beaufort is in blue. During December (Fig. 4A), mean landfast ice width was zero throughout much of the study region and both datasets generally agree where landfast ice had not yet formed. However, where landfast was present (primarily in the Beaufort region), the InSAR-derived results tend

to underestimate the width. On average in the Beaufort region during December the coherence method measured 5.1 km less landfast ice at each coast vector. This is illustrated by the tendency of the blue line to lie below the black line, where the black line indicates a difference of 0 in Figure 4A.

There is a similar pattern for the month of January (Fig. 4B), with the InSAR-based approach still tending to underestimate the width of landfast ice as it expands throughout both study regions. The tendency to underestimate persist until mid-winter, February, March, and April, where the relationship becomes more variable along the coast, with the InSAR-based approach indicating over 10 km more landfast ice than the EM2025 dataset at certain coast vectors (Fig. 4C-E). Although the average differences remain negative during the mid-winter months, with values of -5.1 km, -4.6 km, and -3.4 km from February to April in the Beaufort region, and -2.5 km, -3.7 km, and -1.5 km in the Chukchi region, these differences constitute only small percentages of the total average landfast ice during this period. Also, there is notable spatial variability within the subregion Inner Kotzebue Sound during these months, with the difference in landfast ice width changing from <-10 km to >10 km and back again over the span of just a few coast vectors. The cause of this variability is not certain, but examination of the parent SAR imagery and interferograms over Kotzebue Sound indicate that the surface of the ice loses coherence temporarily without any substantial horizontal motion. This coherence loss could be caused by surface flooding, which has been observed to be caused by heavy snow load in this region (Mahoney et al., 2021). Kotzebue Sound also has extensive areas of shallow water ($\sim\leq$2 m), in which the ice can repeatedly interact with the seafloor as the water level rises and falls under the influence of winds and tides. This process can result in flexure fracturing of the ice surface, which can also lead to coherence loss. Similar observations of poor coherence using C-band SAR over Kotzebue sound were made by Dammann et al. (2019).

In the month of May (Fig. 4F), the landfast ice width difference between the two datasets is more consistently negative. In the Beaufort region the coherence based method measured on average 10.7 km less landfast ice extent during May. Similarly the in the Chukchi region the coherence method measured 5.4 km less than the EM2025. The differences are due to extensive areas where no landfast ice was identified by the coherence-based method, but landfast ice was still present in both the Chukchi and Beaufort coasts in the EM2025 dataset. In particular, Kotzebue Sound never met the coherence threshold to be considered landfast ice during May of any season from 2017-2021. Surface melting is the likely cause of this underestimate and highlights the limitations of using coherence to identify landfast ice outside of the winter months.

3.2 Monthly mean apparent strain

Although there is considerable variability in monthly mean ϵ_a at the scale of adjacent pixels, we identify an overall tendency for lower ϵ_a values to be found near the coast and higher values to occur nearer the SLIE (Fig. 5 and 6). This spatial distribution becomes more evident as the landfast ice season progresses and another tendency emerges whereby the apparent strain in landfast ice tends to decrease over time. Both Figure 5 and 6 are a representation of the mean seasonal progression of landfast ice extent and apparent strain values within the study region. The inset of each figure, denoted by a lowercase A, is a zoomed in view near Utqiagvik, Alaska. Dark blue areas indicate very stable landfast ice, low apparent strain, while yellow indicates relatively less stable landfast ice, high apparent strain (Fig. 5 and 6). The transition from yellow to green to blue, high to low apparent strain, within Elson lagoon throughout the winter months indicates an increase in stability the longer the landfast ice

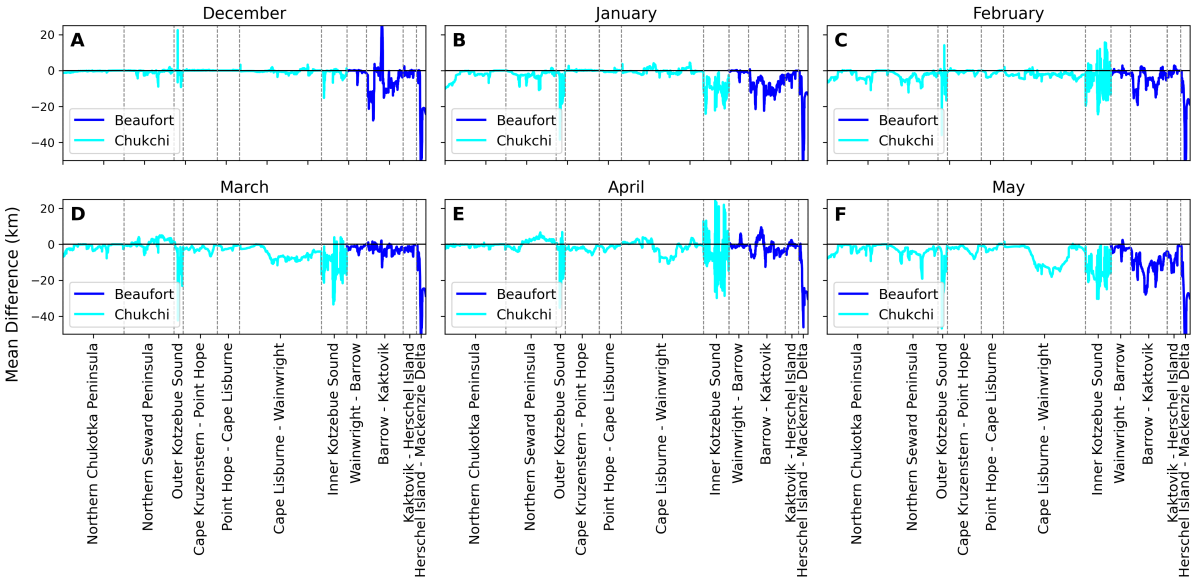

Figure 4. Difference of monthly average landfast ice width measured by the EM2025 dataset and the coherence-based method from 2017-2021 in December through May. Negative values indicate an under estimate by the coherence-based method. Cyan indicated the measurements occurred in the Chukchi region while blue is the Beaufort region. Vertical dashed gray lines indicate the bounds of the subregions shown in Figure 1.

persists (Fig. 5Aa-Ca and 6Aa-Ca). By calculating probability distribution of monthly ϵ_a values , we find that the modal value of ϵ_a decreases monotonically from December to May (Fig. 7). During the month of May, very few pixels within the Chukchi region met the coherence threshold (Fig. 6C). And in both regions, areas of landfast ice did not meet the coherence threshold to be considered landfast ice during the month of June thus the distributions were omitted. The inability to identify landfast ice during formation and after the onset of melt is a major flaw with this method, however the method works throughout the winter months as demonstrated proving the usefulness.

3.3 Quantitative classification of landfast ice stability

In the Beaufort Sea, landfast ice typically reaches its seasonal maximum width during April (Mahoney et al., 2014). This is also the month for which Dammann et al. (2019) qualitatively defined landfast ice stability throughout the Arctic based on interferometric phase gradient. Hence, we use our monthly mean ϵ_a values for the month of April to derive the probability distributions of ϵ_a within the three stability zones identified in Figure 2. The distributions of apparent strain in each stability zone bottomfast (orange), sheltered (blue), and not sheltered (black) are shown in Figure 8). The bottomfast region has a bimodal distribution while the sheltered and not sheltered zones have a well-defined and distinct modes. The modal apparent strain value for the bottomfast ice mask is the lowest and the not-sheltered ice is the highest. The bimodal distribution of apparent strain values within the bottomfast stability zone is likely the associated with tide cracks, which form at the oceanward

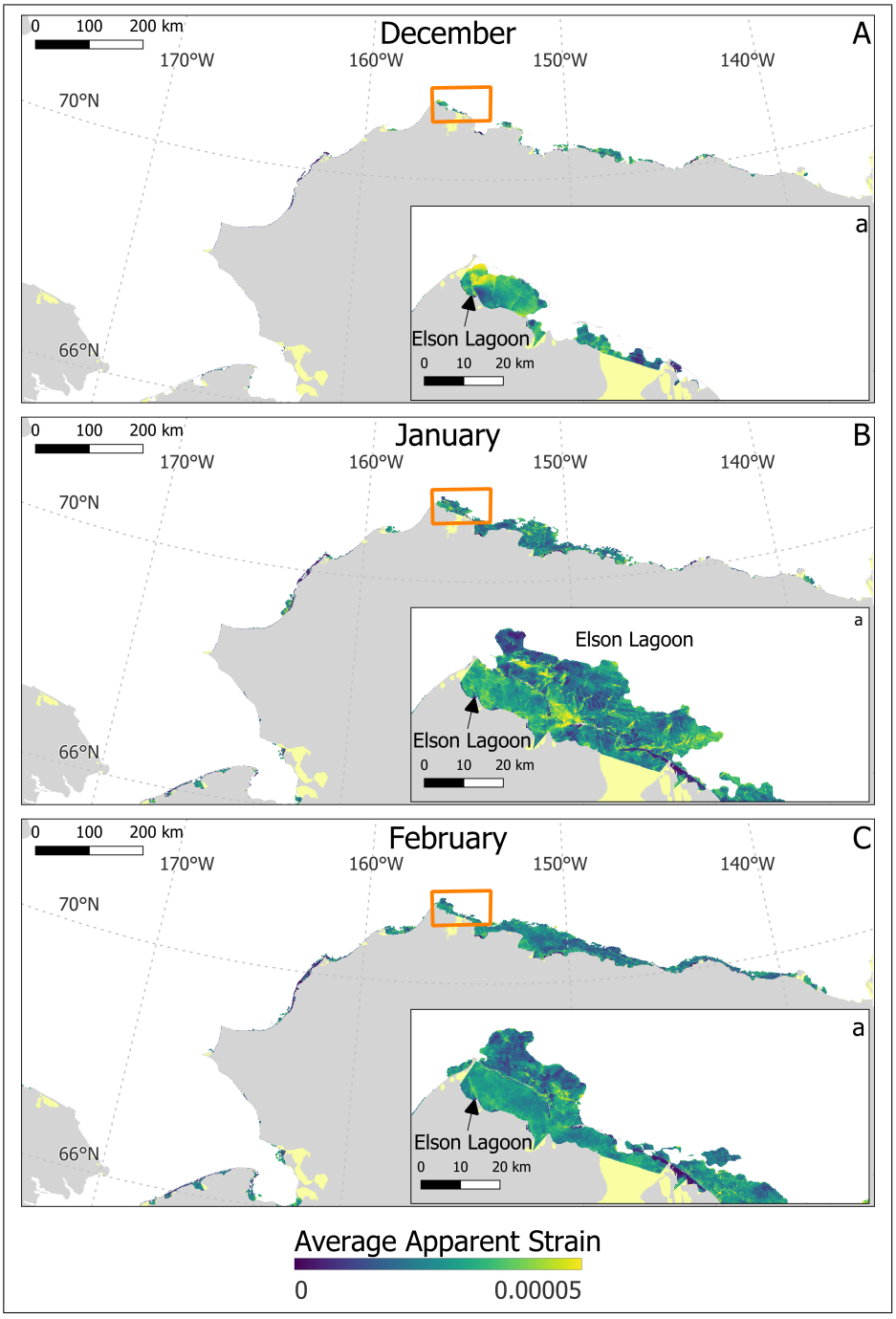

Figure 5. Monthly mean apparent strain values for December (A), January (B), and February (C) for both Beaufort and Chukchi regions from 2017-2021. The orange box denotes the extent of inset figure in each (a). Dark blue areas mark low apparent strain regions while yellow denotes high apparent strain.

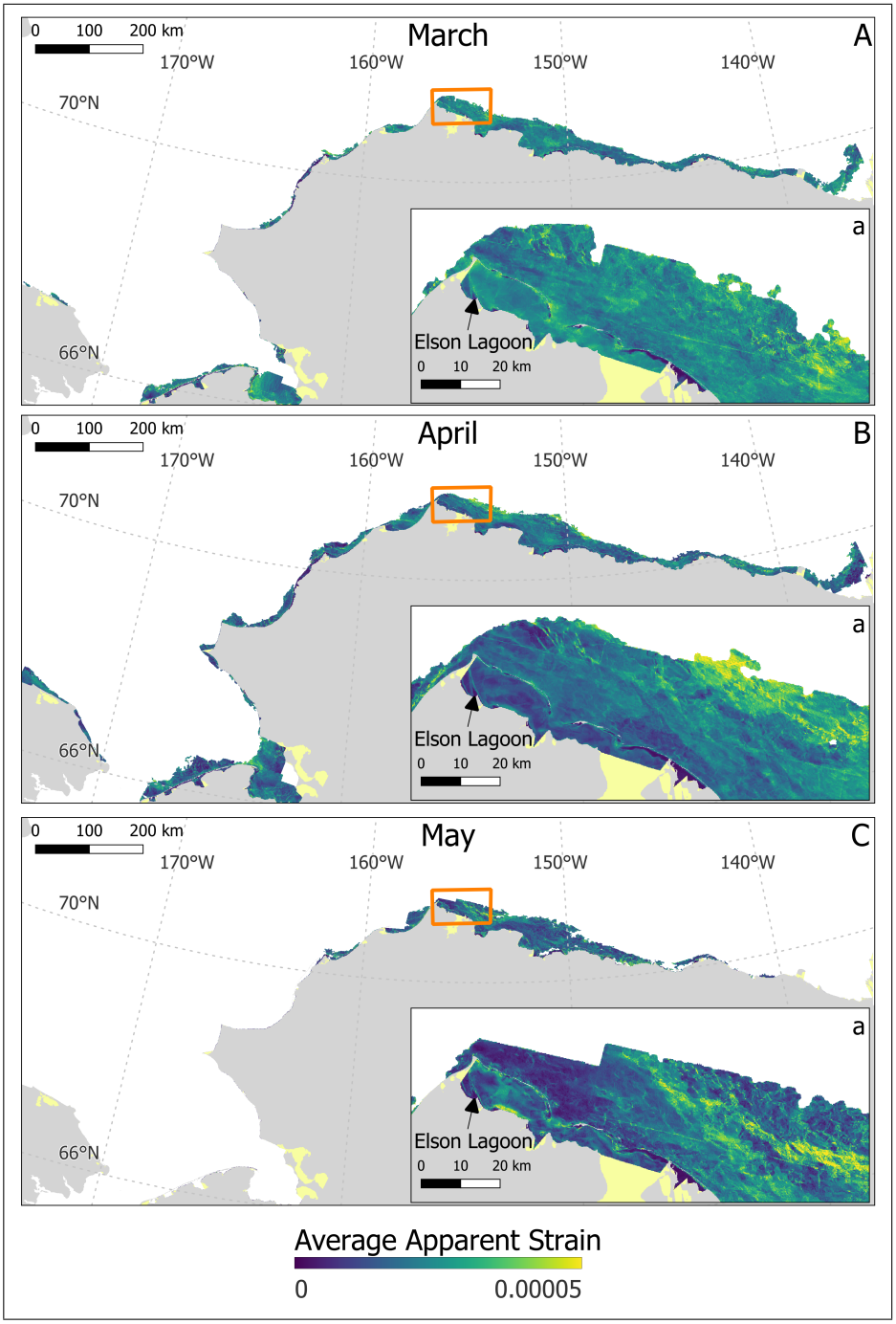

Figure 6. Monthly mean apparent strain values for March (A), April (B), and May (C) for both Beaufort and Chukchi regions from 2017-2021. The orange box denotes the extent of inset figure in each (a). Dark blue areas mark low apparent strain regions while yellow denotes high apparent strain.

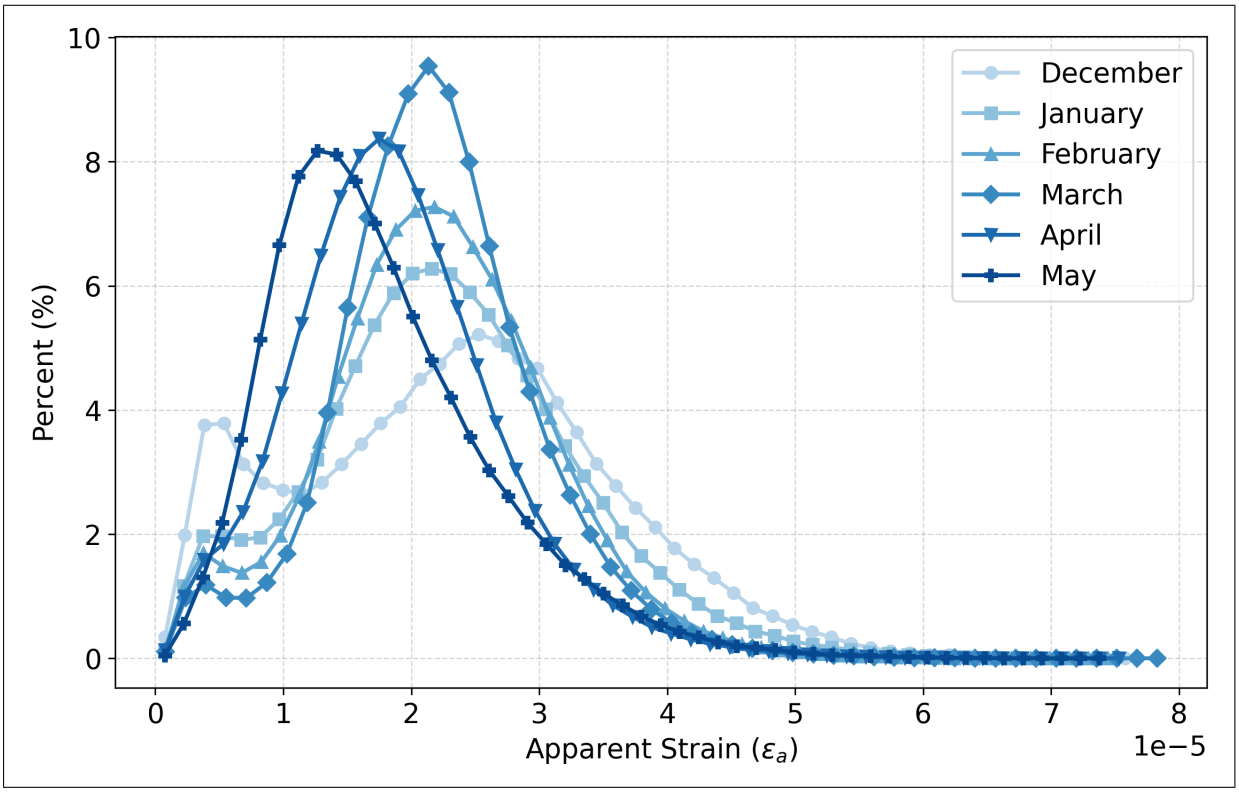

Figure 7. Distribution of the monthly mean apparent strain values from December through May for all pixels within the study region from 2017-2021.

boundary of bottomfast ice. The distributions for sheltered and not-sheltered ice are approximately normally distributed with considerable overlap which is expected as we assume the not sheltered region contains landfast ice which is stabilized by grounded ridges. We then applied Otsu's algorithm (Otsu, 1979) to the distributions of apparent strain in each stability zone independently to determine the apparent strain thresholds associated with each stability zone. The apparent strain threshold for the bottomfast ice stability zone was determined to be $\epsilon_a = 8.6 \times 10^{-6}$, marked by a yellow dashed line in Figure 8. For the sheltered and not sheltered regions the thresholds were determined to be $\epsilon_a = 1.8 \times 10^{-5}$ and $\epsilon_a = 2.4 \times 10^{-5}$ marked by blue and black dashed lines respectively (Fig. 8). However, we only need a single threshold to differentiate sheltered from not sheltered landfast ice. As we have assumed that stabilized landfast ice exists within the not sheltered region, stabilized by grounded ridges, we interpret the Otsu threshold for the not sheltered region to represent the apparent strain threshold for delinting landfast ice which is stabilized by a feature (i.e. barrier island or grounded ridge) and the nonstabilized landfast ice. We now have two apparent strain thresholds that determine the apparent strain bounds for three stability classes:

1. Bottomfast: $\epsilon_a \leq 8.6 \times 10^{-6}$
2. Stabilized: $8.6 \times 10^{-6} < \epsilon_a \leq 2.4 \times 10^{-5}$

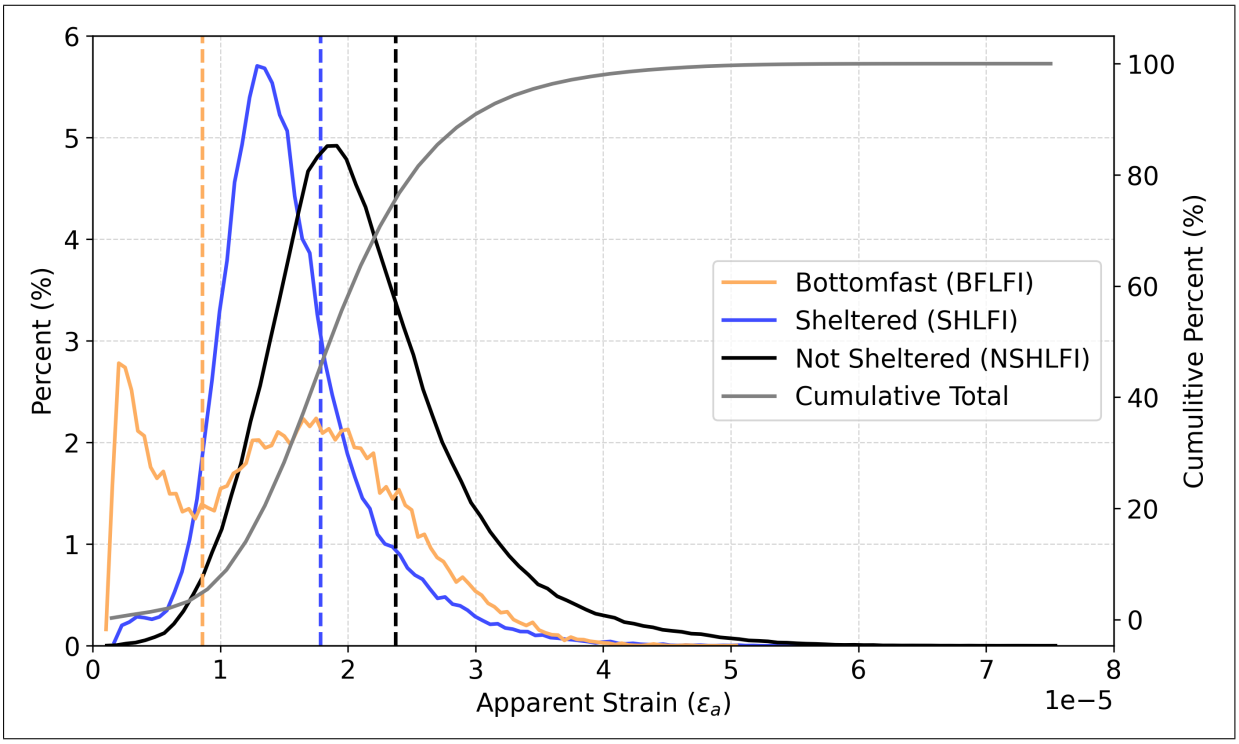

Figure 8. Distribution of the average apparent strain values from April 2017-2021 in each stability zone defined in Figure 2(solid lines). Dashed lines indicate the value of the Otsu threshold for each stability zone.

3. Nonstabilized: $\epsilon_a > 2.4 \times 10^{-5}$

To test our apparent strain thresholds, we calculated the apparent strain of the interferograms used by Dammann et al. (2019) along the Beaufort coastline and compared the extents of our quantitatively defined stability classes to those defined by Dammann et al. (2019). Apart from the method of stability classification, qualitative by Dammann et al. (2019) vs quantitative, Dammann et al. (2019) did not enforce a strict temporal baseline for the SAR pairs and they used a non-zero coherence value to identify the seaward landfast ice edge (SLIE). The three Sentinel-1 SAR pairs used by Dammann et al. (2019) were: April 8th, 2017 – May 2nd, 2017; April 15th, 2017 – May 9th, 2017; and April 17th, 2017 – April 29th, 2017. The interferograms produced from these SAR pairs and the resulting apparent strain maps can be seen in Figures 9A/B. The interferograms show the extents of the stability zones defined by Dammann et al. (2019) with the areas outlined by red identified as bottomfast, purple stabilized and cyan nonstabilized (Fig. 9A). Once the thresholds were applied to the apparent strain maps we directly compared how the qualitative and quantitative methods compared (Fig. 9C). The main difference between the methods is the extent of the nonstabilized landfast ice. The higher coherence threshold used in this study, $\gamma \geq 0.3$, compared to the non-zero requirement by Dammann et al. (2019), resulted in an underestimate of the landfast ice extent. However, the transition from stabilized to nonstabilized is captured well (Fig. 9Ca). In addition, the areas which are classed as bottomfast are separated from

near by stabilized landfast ice by a thin area of nonstabilized ice. We believe this area of high apparent strain is associated with tide cracks as they present as high strain over a relatively short area. To further investigate the performance of the apparent strain thresholds, we produced a confusion matrix of the classification types by Dammann et al. (2019) vs this studies apparent strain classes (Table 1). The nonstabilized class is the only class where both methods agreed on the majority of pixels which met the ≥ 0.3 coherence threshold (Table 1). We believe the classification disagreement, where the apparent strain indicated bottomfast ice while Dammann et al. (2019) stabilized is the result of multiple grounded ridges in a small area. Both of the regions of large misclassifications, west of the Colville Delta and north of Prudhoe Bay (Fig. 9C), have been identified as common areas for grounded ridges to occupy (Lange et al., 2024). Thus we do not view the disagreement of classification as wrong, just that there are various processes can reduce apparent strain, and in the right conditions, produce very stable landfast ice.

	Apparent Strain Class		
Dammann et al. Class	Bottomfast	Stabilized	Nonstabilized
Bottomfast	41.8	33.4	24.8
Stabilized	28.1	46.6	25.3
Nonstabilized	3.6	22.8	73.6

Table 1. Percentages of landfast ice classification types the based on qualitative characteristics by Dammann et al. (2019) and apparent strain thresholds for SAR pairs displayed in Figure 9A.

4 Discussion

4.1 Suitability of InSAR for routine identification of landfast sea ice

In general, landfast ice extent is captured well using interferometric coherence during the winter months of the landfast ice season but under-identifies landfast ice extent at the beginning or end of the season. Despite the typical presence of landfast in both the Chukchi and Beaufort regions during November and June (Mahoney et al., 2024; Mahoney and Einhorn, 2025), we did not find any pixels outside the land mask with a coherence values ≥ 0.3 until December or after May. The coherence-based method does not capture landfast ice extent during the begging and end of the landfast ice season, two important parts of the season when discussing changes between seasons. In the early winter, we attribute the loss of coherence over immobile landfast ice to the rapid changes in the dielectric properties of the ice surface that occurred during early stages of growth (e.g., Winebrenner et al. (1996)). During the months of December and January, the average monthly width of landfast ice identified by our coherence based method under represents compared to the EM2025 dataset from 2017-2021 (-5.1 km in the Beaufort and -0.5 in the Chukchi). Much of the difference in the Beaufort region occurs, between Point Barrow and Kaktovik where our InSAR-derived results show the landfast ice is consistently 6-10 km narrower. In the Chukchi region, differences between InSAR-derived width and EM2025 monthly mean width occur primarily in Kotzebue Sound. Similar to the area between Point

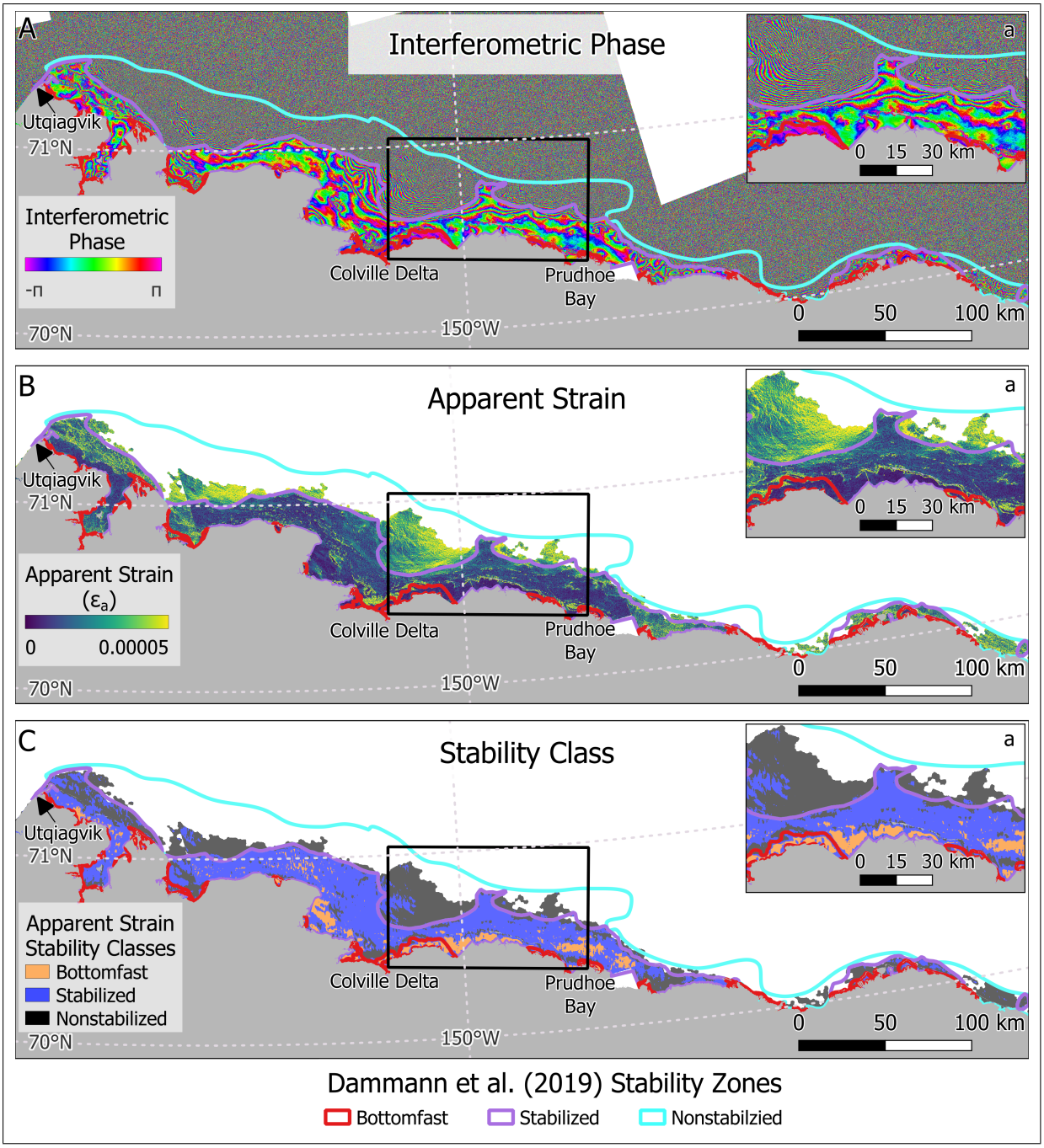

Figure 9. Spatial representation of the interferogram (A), apparent strain (B), and apparent strain derived stability classes (C) compared to the stability zones defined by Dammann et al. (2019) using the same SAR pairs. The black box indicates the location of the inset (a).

Barrow and Kaktovik in the Beaufort region, the InSAR-derived width was on average 8.2 km less than the EM2025 width in Kotzebue Sound during January.

Agreement between InSAR-derived landfast ice extent and the EM2025 dataset is best from February through April. In February through April, our InSAR-based method still slightly underestimated landfast ice width compared to the EM2025 dataset by an average of 2.5 km and 4.4 km, respectively for the combined Chukchi and Beaufort regions. During these months, there are areas where the coherence based method overestimated the landfast ice extent. Specifically, during April north of the Colville Delta (Fig. 3 the coherence-based SLIE is 1-2 km further offshore than the EM2025. This is an area identified as a node (Mahoney et al., 2014) and in proximity to grounded ridges (Lange et al., 2024). Finally, in May, the InSAR based method under measured the landfast ice width consistently across the study region. The consistent under measuring of landfast ice in May is attributed to surface melting causing a loss of coherence between acquisitions. Overall, the coherence-based identification of landfast ice measures the landfast ice width well however the there are certain areas where the combination of 12 days between acquisitions and C-band SAR prevent the methods from identifying landfast ice. On this basis, we find that 12-day repeat Sentinel-1 InSAR may be a useful tool for helping discriminate landfast ice sea ice extent during the coldest months of the year when the dielectric properties of the ice surface are most stable. With the imminent launch of the NISAR satellite, the we hypothesis combination of a 12-day repeat orbit with a L-Band sensor will improve the retention of coherence over landfast ice in the Arctic. In addition, NISAR might allow for coherence to be maintained over Antarctic landfast ice, something C-band is unable to do on a 12-day repeat orbit. Meyer et al. (2011) showed that L-band coherence could be maintained for 45 days over landfast ice and so we anticipate that NISAR may allow us to extend the useful season of InSAR for this landfast ice detection.

4.2 Regional variability and annual evolution of landfast ice stability

We have shown that, over the study area, the distribution of apparent strain evolves such that the modal value of ϵ_a decreases monotonically from December to May across the whole study region (7. We interpret this to indicate that landfast ice becomes more stable the longer it remains in place over winter. To better understand the processes likely to responsible for this, we partitioned this analysis between the 11 subregions shown in Figure 1 and calculated the distribution of monthly mean apparent strain in each subregion (Fig 10). Similar to the study region as a whole, the mode of the apparent strain distribution decreases monotonically from month to month, such that landfast ice transitions toward more stable categories over time in most subregions (Fig. 10). Subregion 9, Point Barrow to Kaktovik (Fig. 10), is the best representation of the evolution of apparent strain in a subregion throughout the year due to the extensive amount of landfast ice and the variety of coastline types. It should be noted that, from December to April, this increase in stability occurs while the overall extent of landfast ice also increases, suggesting that the process by which the SLIE advances also increases the stability of the ice overall. In some subregions, the total landfast ice extent in May is less than that in April, so any increase in the modal ϵ_a value between these two months likely indicates that the least stable landfast ice is the first to detach. However, not all subregions follow a monotonic decrease in apparent strain throughout the season.

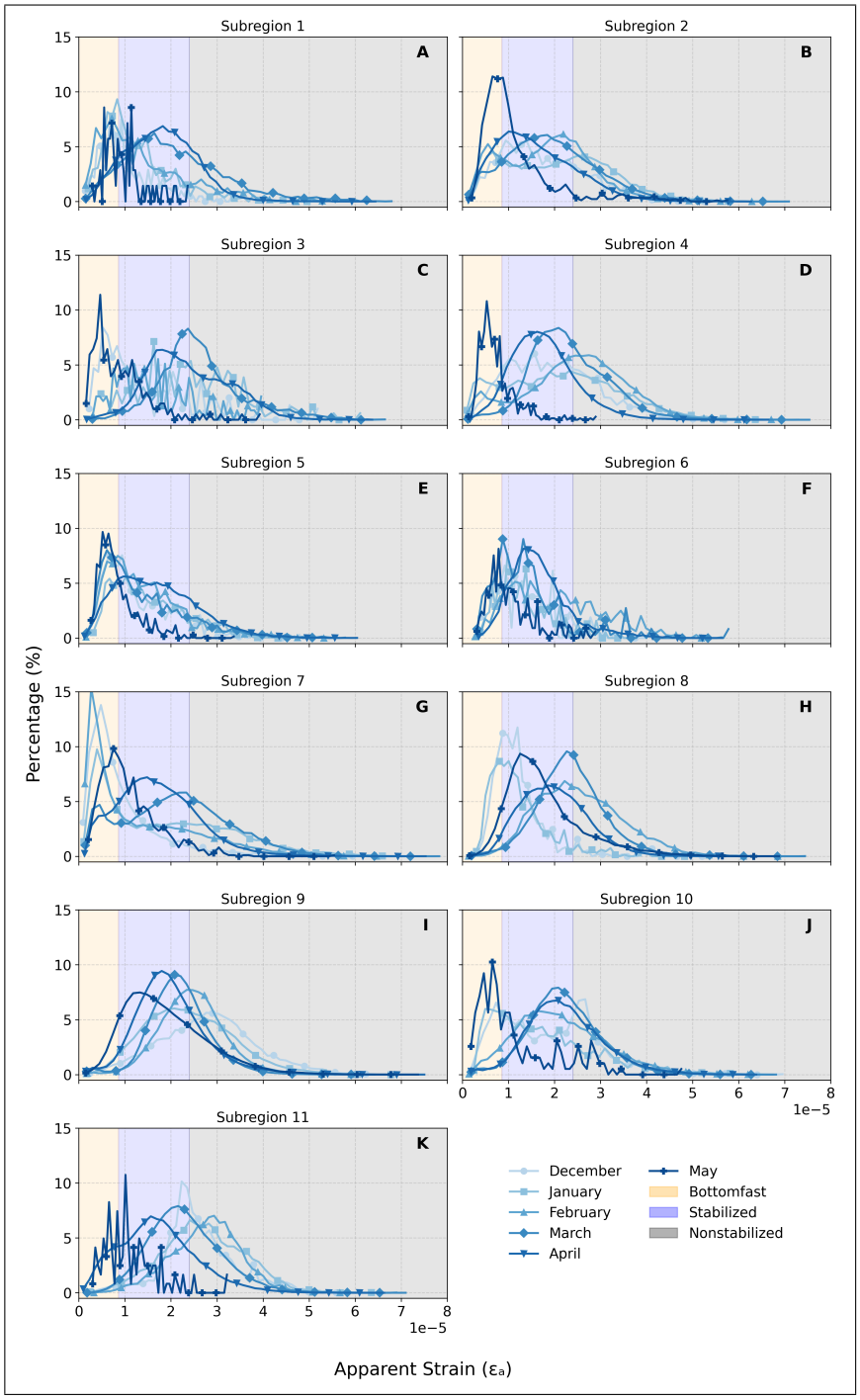

Figure 10. Distributions of monthly apparent strain in the 11 subregions described in Figure 1. Each month form December through May is shown is darker shades of blue as it goes from December to May. Shaded regions indicate the apparent strain values associated with each stability class: orange is bottomfast, blue is stabilized, and gray is nonstabilized

Subregions with extensive lagoon systems have different trends of apparent strain distributions throughout the season. Subregion 1 - Northern Chukotka Peninsula, Subregion 2 - Northern Seward Peninsula, and Subregion 7 - Point Hope to Wainwright are regions where the coastline is primarily composed of lagoons. The landfast ice within these lagoons forms prior to landfast ice outside of the lagoons. During the months when fast ice only exists within a lagoon, the distribution indicated a lower apparent strain mode. In this instance, all the landfast ice is being stabilized by the barrier island, and depending on the depth of the water and the thickness of the ice, it could be bottomfast. The distribution of apparent strain within Subregion 7 (Fig. 10G),is a prime example of the distribution in a subregion dominated by lagoons. The monthly distributions are concentrated within the bottomfast class in the early months (December-February), then follow a typical seasonal progression in March through May (Fig. 10G). The high percentage of low apparent values in subregion 7 during the early months is due to the landfast ice not existing outside of shallow lagoons (Fig 5A-C). It is not until March, when substantial landfast ice exists outside of the shallow lagoons.

4.3 Identification of abrupt increases in apparent strain associated with grounded features

We have shown that the three apparent strain thresholds we defined in section 3.3 for bottomfast, stabilized, and nonstabilized landfast ice align relatively well with the extent of equivalent stability zones identified qualitatively by Dammann et al. (2019) from single interferograms. Within other single-interferogram apparent strain maps, we commonly observe strong gradients in apparent strain that are not evident in the monthly average maps illustrated in Figures 5 and 6 which we believe are associated with the transition from grounded to floating landfast ice. For example, at the seaward edge of the bottomfast ice, there are tide crack zones where the floating landfast ice flexes in response to sea level variations while the bottomfast ice remains stationary. The difference in vertical motion across this narrow region (typically a few 10s of meters wide) leads to a region of high fringe density, like those found at the grounding lines of ice shelves and tidewater glaciers (Friedl et al., 2019), resulting in high apparent strain. Examples of such features can be seen in two apparent strain maps from April 05 - 17, 2017 (Fig.11A) and April 09 - 21, 2022 (Fig. 11B) near Oliktok Point in the Beaufort region. We see abrupt increases of apparent strain in both maps associated with a tide crack, a barrier island, and a grounded ridge (Fig. 11C). During 2022 the landfast ice was more extensive allowing for the formation of a second grounded ridge (Fig. 11C). The resemblance of these features to those around barrier islands leads us to interpret them as the tide crack zone around grounded ridges. Moreover, they occur at the locations grounded ridges have been identified in this region during the 2021-22 landfast ice season by Lange et al. (2024). In addition, similar patterns in apparent strain values can be observed on within the lagoon and oceanward of the barrier island, providing further evidence the abrupt gradient in apparent strain is associated with a stabilizing feature.

The shoreward feature identified as a grounded ridge occurred in approximately the same location in both 2017 and 2022, but the apparent strain patten deviates offshore of this location around 23 km. Both transects indicate a reduction of apparent strain offshore of the seaward grounded ridge (Fig. 11C). We believe this to to be the local stabilized affect of a grounded feature. However proving and interpreting this is outside the scope of this study. It is also possible the areas high apparent strain gradients are not the grounded features, but the low apparent strain features about these areas. A direct comparison to

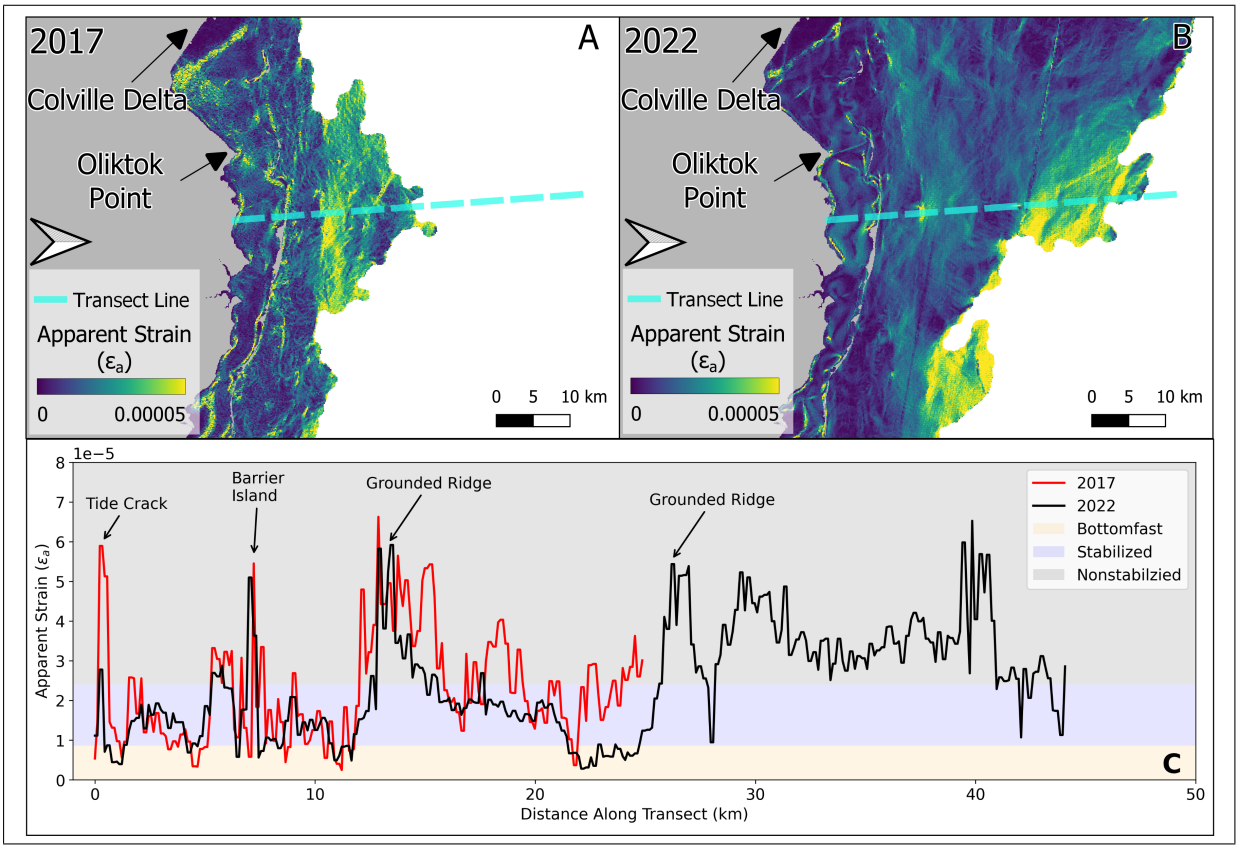

Figure 11. Apparent strain maps from April 2017 (A) and April 2022 (B) and the associated apparent strain values along a transect near Oliktok Point, Alaska (C). Apparent strain values along each transect (2017 red, and 2022 black) can be sorted into stability classes and used to identify the location of features.

the location of the grounded ridges by Lange et al. (2024) could provide evidence of the apparent strain pattern related to the grounded features versus the fast ice surrounding the ridge.

5 Conclusion

InSAR-based methods hold great promise for improving our understanding of both the spatial extent of landfast sea ice and its relative stability. Meyer et al. (2011) already demonstrated the usefulness of interferometric coherence in delineating landfast ice from the mobile pack ice using 45-day repeat L-band PALSAR data. Our investigation shows that a similar approach with a coherence threshold for C-band can work well during the winter months and throughout most of our study area using 12-day C-band Sentinel-1 data. During the winter months, February - April, landfast ice widths derived from coherence threshold approach typically agreed to within a few km, of those derived from the EM2025 dataset (Fig 4C-E). However, factors unrelated to the motion of the ice reduce coherence at the beginning and end of the season, occasionally resulting in false absence of

landfast ice (corresponding to a 100% underestimate in Figure 4E and F, for example). Hence, the usefulness of out interferometric coherence method for identifying landfast ice would be improved with either a shorter period between SAR images or a use of longer radar wavelength. We therefore look forward to the launch of the NASA-ISRO synthetic aperture radar (NISAR) currently scheduled to launch in 2025. The L-band sensor and 12-day repeat interval should open new opportunities for routine mapping of landfast extent using InSAR.

In a quantitative expansion the work done by Dammann et al. (2019), we find apparent strain, ϵ_a, can serve as a meaningful measure landfast ice stability. Specifically, we find that the distributions of ϵ_a values within the bottomfast ice zone and either seaward or shoreward of barrier islands have distinct modes. This allows us to define three landfast ice stability classes on the basis of apparent strain: bottomfast ice ($\epsilon_a \leq 8.6 \times 10^{-6}$), stabilized ($8.6 \times 10^{-6} < \epsilon_a \leq 2.4 \times 10^{-5}$), and nonstabilized ($\epsilon_a > 2.4 \times 10^{-5}$). Single interferograms indicate a spatially abrupt change in apparent strain between the stabilized and non-stabilized landfast ice. These abrupt changes are not present within the monthly average apparent strain images (Fig. 5 and 6). The grounded ridges likely persist between interferograms in the same season. However, they are not present in the monthly averages indicating the the strain field in landfast ice evolves more rapidly than the repeat interval of Sentinel-1 and because the monthly averages combine results from different viewing geometries. Nonetheless, the boundary between stabilized and not stabilized ice is often associated with features that we interpret to be grounded features (Fig. 11), which suggests our classification represents physical difference in the strain experienced by landfast ice on either side. To our knowledge, this is the first time InSAR has been used to identify individual grounded ridges based on localized values of high apparent strain. Our interpretation on this matter is strongly supported by matching the locations of grounded ridges identified by Lange et al. (2024), based on ICESat-2 altimetry data. Moreover, our observations support their findings that grounded ridges are commonly located shoreward of the landfast ice edge.

Along with the establishment of the apparent strain thresholds we defined, we observed a decrease in apparent strain throughout the season. The increase in stability the longer the landfast ice is likely due to thickening, but further investigation into the cause is needed. A fundamental flaw in using information derived from interferometry is the inability of InSAR to capture along-track deformation. Being limited to the magnitude of line-of-sight deformation causes an under representation of the total possible deformation which occurred. Implementing methods to resolve the two-dimensional strain, demonstrated by Fedders et al. (2024) would improve our ability to classify landfast ice stability based on the apparent strain. The ability of InSAR to identify these areas of varying stability can hold immense value to members of Arctic coastal communities such that they can continue to operate on the landfast ice safely.

Code availability. Code for processing of the ASF Vertex outputs into apparent strain can be found here (https://github.com/aheinhorn/Alaska_InSAR_CODE). All the code for analyzing the fast ice extent of the coherence derived width and EM2025 derived width can be found here (https://github.com/armahoney/SLIEalyzer)

Data availability. Sentinel-1 SAR imagery are openly accessible at the Alaska Satellite Facility's Vertex tool (https://search.asf.alaska.edu), where users can search for imagery, request on-demand processing (include InSAR products), and download data. Registration with NASA EarthData is required but is open to anyone. The EM2025 dataset is available through the University of Alaska Fairbanks Scenarios Network for Alaska and Arctic Planning (SNAP) at https://catalog.snap.uaf.edu/geonetwork/srv/eng/catalog.search#/metadata/a6323019-0023-4e0d-98dc-a01b13b the Chukchi region) and https://catalog.snap.uaf.edu/geonetwork/srv/eng/catalog.search#/metadata/5adee563-786d-4b54-bbec-56dea055ec9a (for the Beaufort region) under a Creative Commons license (CC-BY 4.0)

Author contributions. All authors edited the manuscript. AHE led the analysis, produced figures, and drafted the article. ARM created the SLIEalizer package and provided scientific and editorial feedback and direction to the project.

Competing interests. The authors declare that they have no conflict of interest.

Disclaimer. The views and conclusions contained on the website are those of the authors and should not be interpreted as representing the opinions or policies of the US Government, nor does mention of trade names or commercial products constitute endorsement or recommendation for use.

Acknowledgements. Study collaboration and funding were provided by the US Department of the Interior, Bureau of Ocean Energy Management (BOEM), Environmental Studies Program, Washington, DC, under Agreement Number M19AC00021. We are also extremely grateful to the members of our Science Review Board, Hajo Eicken, Andrew Roberts, and John Walsh Study collaboration and funding were provided by the US Department of the Interior, Bureau of Ocean Energy Management (BOEM), Environmental Studies Program, Washington, DC, under Agreement Number M19AC00021

References

Bamler, R. and Hartl, P.: Synthetic aperture radar interferometry, Tech. rep., 1998.

Barry, R. G., Moritz, R. E., and Rogers, J. C.: The fast ice regimes of the Beaufort and Chukchi Sea coasts, Alaska, Cold Regions Science and Technology, 1, https://doi.org/10.1016/0165-232X(79)90006-5, 1979.

Bieniek, P. A., Eicken, H., Jin, M., Mahoney, A. R., Jones, J., and Bhatt, U. S.: Seasonal forecasting of landfast ice in Foggy Island Bay, Alaska in support of ice road operations, Cold Regions Science and Technology, 201, https://doi.org/10.1016/j.coldregions.2022.103618, 2022.

Cooley, S. W. and Ryan, J. C.: Community-scale changes to landfast ice along the coast of Alaska over 2000-2022, Environmental Research Letters, 19, https://doi.org/10.1088/1748-9326/ad1c7b, 2024.

Dammann, D. O., Eicken, H., Meyer, F. J., and Mahoney, A. R.: Assessing small-scale deformation and stability of landfast sea ice on seasonal timescales through L-band SAR interferometry and inverse modeling, Remote Sensing of Environment, 187, 492–504, https://doi.org/10.1016/j.rse.2016.10.032, 2016.

Dammann, D. O., Eicken, H., Mahoney, A. R., Meyer, F. J., Freymueller, J. T., and Kaufman, A. M.: Evaluating landfast sea ice stress and fracture in support of operations on sea ice using SAR interferometry, Cold Regions Science and Technology, 149, 51–64, https://doi.org/10.1016/j.coldregions.2018.02.001, 2018a.

Dammann, D. O., Eriksson, L. E. B., Mahoney, A. R., Stevens, C. W., van der Sanden, J., Eicken, H., Meyer, F. J., and Tweedie, C. E.: Mapping Arctic Bottomfast Sea Ice Using SAR Interferometry, Remote Sensing, 10, https://doi.org/10.3390/rs10050720, 2018b.

Dammann, D. O., Eriksson, L. E. B., Mahoney, A. R., Eicken, H., and Meyer, F. J.: Mapping pan-Arctic landfast sea ice stability using Sentinel-1 interferometry, Cryosphere, 13, 557–577, https://doi.org/10.5194/tc-13-557-2019, 2019.

Dammert, P. B., Lepparanta, M., and Askne, J.: SAR interferometry over baltic sea ice, International Journal of Remote Sensing, 19, 3019–3037, https://doi.org/10.1080/014311698214163, 1998.

Danielson, S. L., Dobbins, E. L., Jakobsson, M., Johnson, M. A., Weingartner, T. J., Williams, W. J., and Zarayskaya, Y.: Sounding the Northern Seas, EOS, 96, https://eos.org/science-updates/sounding-northern-seas, 2015.

Fedders, E., Mahoney, A., Dammann, D. O., Polashenski, C., and Hutchings, J.: Two-dimensional thermal and dynamical strain in landfast sea ice from InSAR: results from a new analytical inverse method and field observations, Annals of Glaciology, 65, 1–14, https://doi.org/https://doi.org/10.1017/aog.2024.29, 2024.

Ferretti, A., Monti-Gaurnieri, A., Prati, C., and Rocca, F.: lnSAR Principles: Guidelines for SAR lnterf erometry Processing and Interpretation, vol. TM-19, ESA Publications, 2007.

Fraser, A. D., Massom, R. A., Michael, K. J., Galton-Fenzi, B. K., and Lieser, J. L.: East antarctic landfast sea ice distribution and variability, 2000-08, Journal of Climate, 25, 1137–1156, https://doi.org/10.1175/JCLI-D-10-05032.1, 2012.

Fraser, A. D., Massom, R. A., Ohshima, K. I., Willmes, S., Kappes, P. J., Cartwright, J., and Porter-Smith, R.: High-resolution mapping of circum-Antarctic landfast sea ice distribution, 2000-2018, Earth System Science Data, 12, 2987–2999, https://doi.org/10.5194/essd-12-2987-2020, 2020.

Fraser, A. D., Massom, R. A., Handcock, M. S., Reid, P., Ohshima, K. I., Raphael, M. N., Cartwright, J., Klekociuk, A. R., Wang, Z., and Porter-Smith, R.: Eighteen-year record of circum-Antarctic landfast-sea-ice distribution allows detailed baseline characterisation and reveals trends and variability, Cryosphere, 15, 5061–5077, https://doi.org/10.5194/tc-15-5061-2021, 2021.

Friedl, P., Weiser, F., Fluhrer, A., and Braun, M. H.: Remote Sensing of Glacier and Ice Sheet Grounding Lines: A Review 2, 2019.

George, J. C., Zeh, J., Suydam, R., and Clark, C.: Abundance and population trend (1978-2001) of western arctic bowhead whales surveyed near Barrow, Alaska, https://doi.org/10.1111/j.1748-7692.2004.tb01191.x, 2004.

Hogenson, K., Arko, S., Buechler, B., Hogenson, R., Herrmann, J., and Geiger, A.: Hybrid Pluggable Processing Pipeline (HyP3): A cloud-based infrastructure for generic processing of SAR data, in: AGU Fall Meeting, 2016.

Hošeková, L., Eidam, E., Panteleev, G., Rainville, L., Rogers, W. E., and Thomson, J.: Landfast Ice and Coastal Wave Exposure in Northern Alaska, Geophysical Research Letters, 48, https://doi.org/10.1029/2021GL095103, 2021.

Itkin, P., Losch, M., and Gerdes, R.: Landfast ice affects the stability of the Arctic halocline: Evidence from a numerical model, Journal of Geophysical Research: Oceans, 120, 2622–2635, https://doi.org/10.1002/2014JC010353, 2015.

Laidre, K. L., Stirling, I., Lowry, L. F., Wiig, , Heide-Jørgensen, M. P., and Ferguson, S. H.: QUANTIFYING THE SENSITIVITY OF ARCTIC MARINE MAMMALS TO CLIMATE-INDUCED HABITAT CHANGE, 2008.

Laidre, K. L., Stern, H., Kovacs, K. M., Lowry, L., Moore, S. E., Regehr, E. V., Ferguson, S. H., Wiig, , Boveng, P., Angliss, R. P., Born, E. W., Litovka, D., Quakenbush, L., Lydersen, C., Vongraven, D., and Ugarte, F.: Arctic marine mammal population status, sea ice habitat loss, and conservation recommendations for the 21st century, Conservation Biology, 29, 724–737, https://doi.org/10.1111/cobi.12474, 2015.

Lange, K. A., Bradley, A. C., Duncan, K., Farrell, S. L., and Bradley, A.: Grounded ridge detection and characterization along the Alaskan Arctic coastline using ICESat-2 surface height retrievals, EGUsphere [preprint], https://doi.org/10.5194/egusphere-2024-1885, 2024.

Li, S., Shapiro, L., Mcnutt, L., and Jeffers, A.: Application of Satellite Radar Interferometry to the Detection of Sea Ice Deformation, Journal of the Remote Sensing Society of Japan, 16, 153–163, 1996.

Libert, L., Wuite, J., and Nagler, T.: Automatic delineation of cracks with Sentinel-1 interferometry for monitoring ice shelf damage and calving, Cryosphere, 16, 1523–1542, https://doi.org/10.5194/tc-16-1523-2022, 2022.

Lovvorn, J. R., Anderson, E. M., Rocha, A. R., Larned, W. W., Grebmeier, J. M., Cooper, L. W., Kolts, J. M., and North, C. A.: Variable wind, pack ice, and prey dispersion affect the long-term adequacy of protected areas for an Arctic sea duck, Ecological Applications, 24, 396–412, https://doi.org/10.1890/13-0411.1, 2014.

Mahoney, A., Eicken, H., Graves, A., and Shapiro, L.: DEFINING AND LOCATING THE SEAWARD LANDFAST ICE EDGE IN NORTHERN ALASKA, Int. Conf. on Port and Ocean Eng. Under Arctic Conditions, 3, 991–1000, 2006.

Mahoney, A., Eicken, H., Gaylord, A. G., and Shapiro, L.: Alaska landfast sea ice: Links with bathymetry and atmospheric circulation, Journal of Geophysical Research: Oceans, 112, https://doi.org/10.1029/2006JC003559, 2007.

Mahoney, A., Bieniek, P., Danielson, S., Einhorn, A., Hedstrom, K., Jones, J., and Klenz, T.: Landfast Ice Climatology within the Arctic OCS, 2024.

Mahoney, A. R. and Einhorn, A. H.: The Evolving Decline of Landfast Sea Ice in Northern Alaska and Adjacent Waters: Results from an Updated Climatology, Journal of Geophysical Research - Oceans, In Review, https://doi.org/10.22541/essoar.173939541.17906910/v1, 2025.

Mahoney, A. R., Eicken, H., Gaylord, A. G., and Gens, R.: Landfast sea ice extent in the Chukchi and Beaufort Seas: The annual cycle and decadal variability, Cold Regions Science and Technology, 103, 41–56, https://doi.org/10.1016/j.coldregions.2014.03.003, 2014.

Mahoney, A. R., Turner, K. E., Hauser, D. D. W., Laxague, N. J. M., Lindsay, J. M., Whiting, A. V., Witte, C. R., Goodwin, J., Harris, C., Schaeffer, R. J., Schaeffer, R., Betcher, S., Subramaniam, A., and Zappa, C. J.: Thin ice, deep snow and surface flooding in Kotzebue Sound: Landfast ice mass balance during two anomalously warm winters and implications for marine mammals and subsistence hunting, Journal of Glaciology, 67, 1013–1027, https://doi.org/10.1017/jog.2021.49, 2021.

Masterson, D. M.: State of the art of ice bearing capacity and ice construction, Cold Regions Science and Technology, 58, 99–112, https://doi.org/10.1016/j.coldregions.2009.04.002, 2009.

Meyer, F. J., Mahoney, A. R., Eicken, H., Denny, C. L., Druckenmiller, H. C., and Hendricks, S.: Mapping arctic landfast ice extent using L-band synthetic aperture radar interferometry, Remote Sensing of Environment, 115, 3029–3043, https://doi.org/10.1016/j.rse.2011.06.006, 2011.

Moreira, A., Prats-Iraola, P., Younis, M., Krieger, G., Hajnsek, I., and Papathanassiou, K. P.: A tutorial on synthetic aperture radar, IEEE Geoscience and Remote Sensing Magazine, 1, 6–43, https://doi.org/10.1109/MGRS.2013.2248301, 2013.

Morris, K., Li, S., and Jeffries, M.: Meso- and microscale sea-ice motion in the East Siberian Sea as determined from ERS-1 SAR Data, Journal of Glaciology, 45, 370–383, https://doi.org/10.3189/s0022143000001878, 1999.

Otsu, N.: A Threshold Selection Method from Gray-Level Histograms, IEEE Transactions on System, Man, and Cybernetics, 9, 62–66, https://doi.org/10.1109/TSMC.1979.4310076, 1979.

Pratt, J. W.: Mapping bottomfast sea ice in arctic lagoons using Sentinel-1 interferometery, 2022.

Wang, Z., Liu, J., Wang, J., Wang, L., Luo, M., Wang, Z., Ni, P., and Li, H.: Resolving and analyzing landfast ice deformation by insar technology combined with sentinel-1a ascending and descending orbits data, Sensors (Switzerland), 20, 1–16, https://doi.org/10.3390/s20226561, 2020.

Winebrenner, D. P., Holt, B., and Nelson, E. D.: Observation of autumn freeze-up in the Beaufort and Chukchi Seas using the ERS 1 synthetic aperture radar, Journal of Geophysical Research: Oceans, 101, 16 401–16 419, https://doi.org/10.1029/96JC01292, 1996.

World Meteorological Organization: World Meterological Organization: WMO sea-ice nomenclature, Tech. rep., Geneva, 2014.